

Supporting information for

Construction of 3D Architectures with Ni(HCO₃)₂ Nanocubes Wrapped by Reduced Graphene Oxide for LIBs: Ultrahigh Capacity, Ultrafast Rate Capability and Ultralong Cycle Stability

Yutao Dong, Yuhang Ma, Dan Li, Yushan Liu, Weihua Chen*, Xiangming Feng, and Jianmin

Zhang*

College of Chemistry and Molecular Engineering, Zhengzhou University, Zhengzhou 450001, Henan, China

Corresponding Author

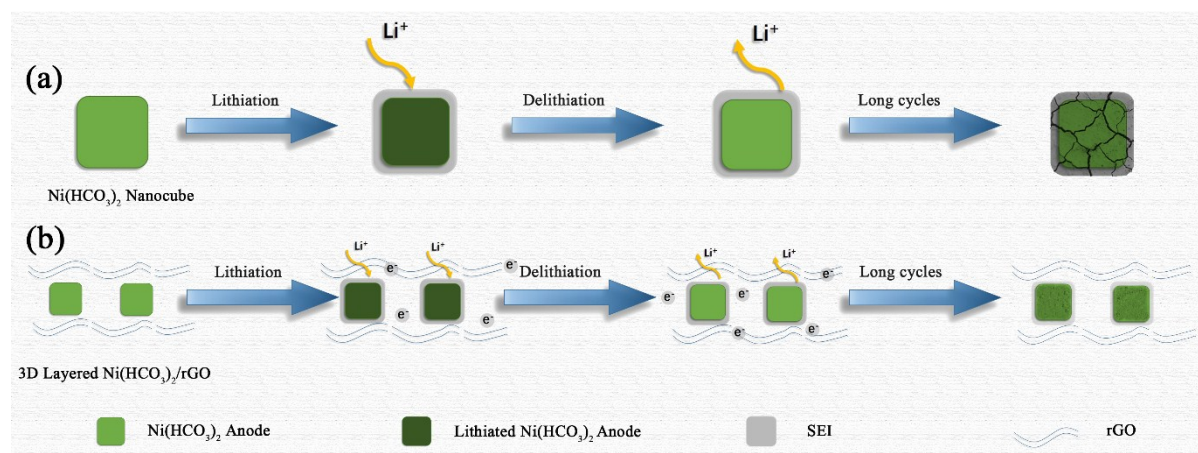
zhjm@zzu.edu.cn, chenweih@zzu.edu.cn

Experimental section

Chemicals: Natural graphite flakes with the average diameter of 200 meshes was purchased from Sigma-Aldrich Co. Ltd. (USA). Nickel acetate tetrahydrate ($\text{CoCl}_2 \cdot 4\text{H}_2\text{O}$), urea, lithium carbonate (Li_2CO_3), nickel oxide (NiO , $d=30\text{nm}$), N-methyl-2-pyrrolidinone (NMP), potassium permanganate (KMnO_4), hydrogen peroxide (H_2O_2), hydrochloric acid (HCl, 37%) and concentrated sulphuric acid (H_2SO_4 , 98%) were analytical grade reagent received from Sinopharm Chemical Reagent Co. Ltd. (Shanghai, China), and used without any further purification. Deionized water was used throughout.

Synthesis of graphene oxide: Graphene oxide (GO) was synthesized using the following modified Hummer's method as reported.¹ Graphite (2 g) was mixed with concentrated H_2SO_4 (69 mL), and the mixture was stirred for 30 min within an ice bath. KMnO_4 (8 g) was added very slowly into the dark suspension and the reaction mixture was stirred and sonicated for another 15 min. Then the ice bath was removed, and the mixture was stirred at 35 °C overnight. Distilled water was added into the pasty solution under magnetic stirring and the color of the solution turned to yellowish brown. After another 2 h of vigorous stirring, H_2O_2 (30 wt.%, 25 mL) was added and the color of the solution turned to golden yellow immediately. The mixture was washed with HCl (5 %) and then deionized water for several times until the solution became acid free. After freeze-drying treatment overnight, the GO was obtained and used for the further experimental work.

Supporting Figures and Tables



Scheme S1 Schematic of the electrochemical process for two configurations of electrodes. (a) Pure $\text{Ni}(\text{HCO}_3)_2$ nanocubes undergo substantial structural expansion, which tends to cause extensive self-aggregation, resulting in poor cycling stability and large irreversible capacity loss. (b) 3D layered rGO films as the buffering framework effectively stabilize the $\text{Ni}(\text{HCO}_3)_2$ nanocubes, resulting in restricting the expansion and reaggregation of $\text{Ni}(\text{HCO}_3)_2$ nanocubes in the discharge/charge process, leading to a long cycle stability and high rate performance.

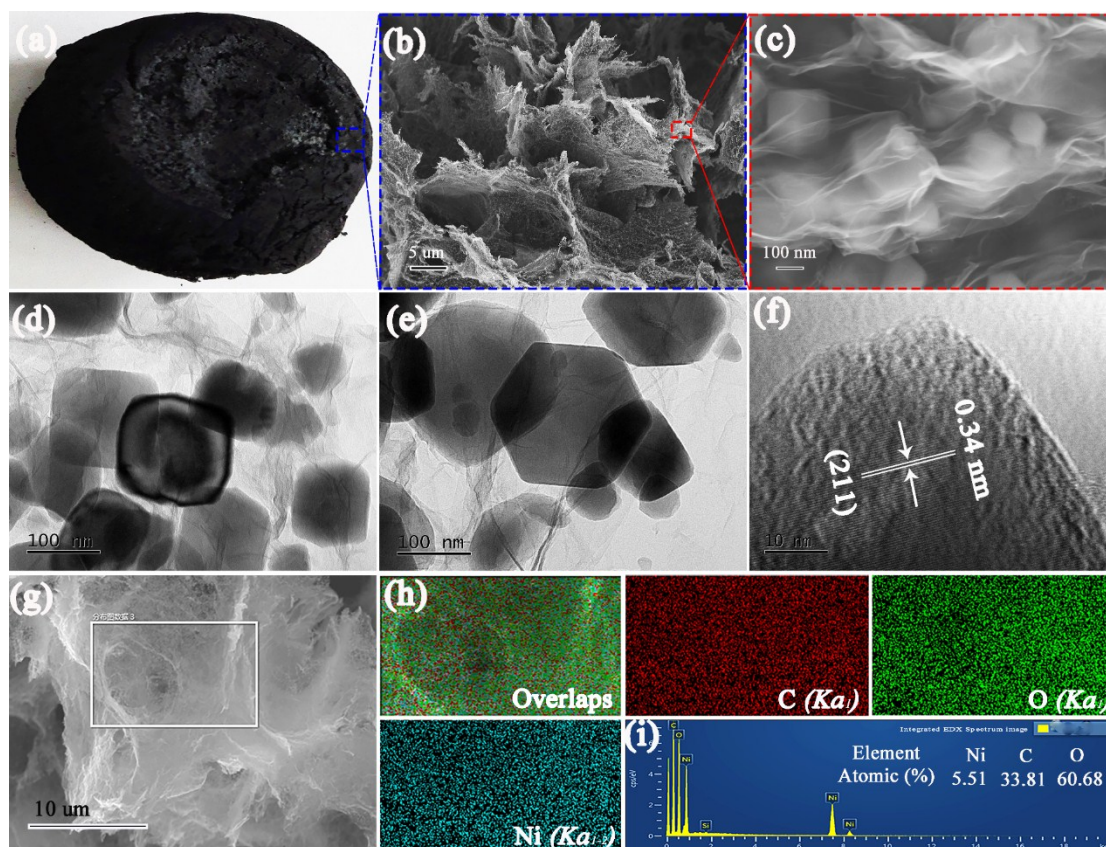


Fig. S1 (a) Black aerogel of $\text{Ni}(\text{HCO}_3)_2/\text{rGO}$, (b,c) SEM images, showing that most of $\text{Ni}(\text{HCO}_3)_2$ nanocubes are embedded in the porous rGO networks; (d,e) TEM images, (f) HRTEM image, (g) SEM image of the selected area and (h) Elemental mapping images, showing the uniform presence of C, O, and Ni; and (i) EDS spectrum.

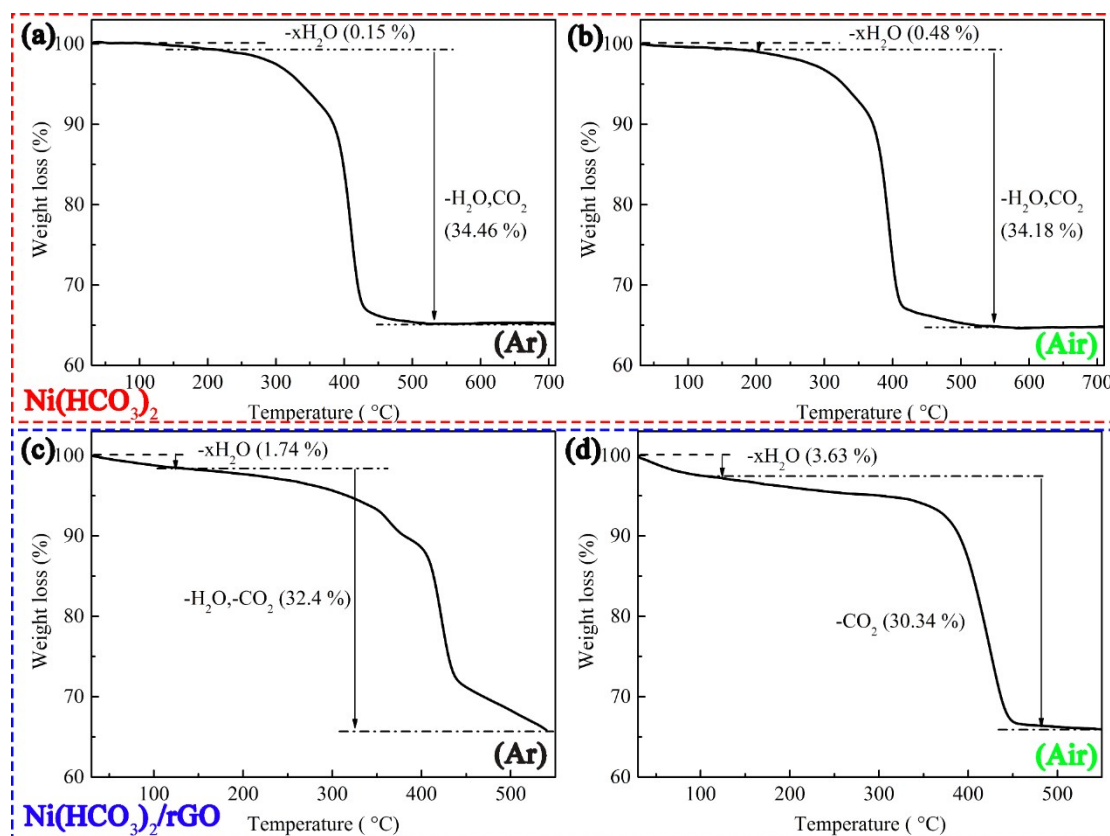


Fig. S2 TGA profiles in Ar and air atmosphere of the (a, b) Ni(HCO₃)₂ without GO, and (c, d) Ni(HCO₃)₂/rGO.

To calculate the carbon (rGO) content in the Ni(HCO₃)₂/rGO composite, first, we tested the TGA of the Ni(HCO₃)₂ without GO in Ar and air atmosphere with a heating rate of 10°C min⁻¹ up to 700°C to investigate its thermal behavior. As shown in Fig.S2a (in Ar atmosphere) and Fig.S2b (in Air atmosphere), the two curves exhibit almost the same two successive declining stages, corresponding to the dehydration and dehydration/decarboxylation processes, respectively. According to Fig.S2a and Fig.S2b, the first stage occurs below 150°C with a weight loss of about 0.15 % and 0.48%, respectively. It can be attributed to the removal of adsorbed water. The second weight loss stage is located in the temperature range of 150-540°C. The weight loss of about 34.46 % and 34.18 %, respectively. It can be ascribed to the decomposition of nickel bicarbonate. The weight have almost no change in the range from 540°C to 700°C for Fig.S2a and Fig.S2b. So, we tested the TGA of the Ni(HCO₃)₂/GO in Ar and then in air atmosphere to get more accurate

content of the carbon (rGO) in the Ni(HCO₃)₂/rGO composite with the same heating rate of 10 °C min⁻¹ up to 540 °C. First, The TGA plot of Ni(HCO₃)₂/rGO (Fig.S2c) was conducted at a heating rate of 10 °C min⁻¹ in Ar atmosphere from room temperature to 540 °C. The slight weight loss before 150 °C is attributed to the release of the physically absorbed water (-1.74 wt.%), and the later weight loss between 150 and 540 °C is assigned to the thermal decomposition of Ni(HCO₃)₂ (-32.4 wt.%). The total weight loss is 34.14% (1.74 % +32.4 %=34.14%). After the heat in Ar atmosphere, the TGA plot of the sample (Fig.S2d) was conducted at a heating rate of 10 °C min⁻¹ in air atmosphere from room temperature to 540 °C. The slight weight loss before 150 °C is attributed to the release of the physically absorbed water (-3.63 wt.%), and the later weight loss between 150 and 540 °C is assigned to the thermal oxidization reaction between rGO and oxygen ($C + O_2 \rightarrow CO_2$) (-30.34 wt.%). From the TGA test, we can calculate the contains of rGO in Ni(HCO₃)₂/rGO (30.34 %*(1-34.14%) = 19.98 %) is 19.98 wt.%.

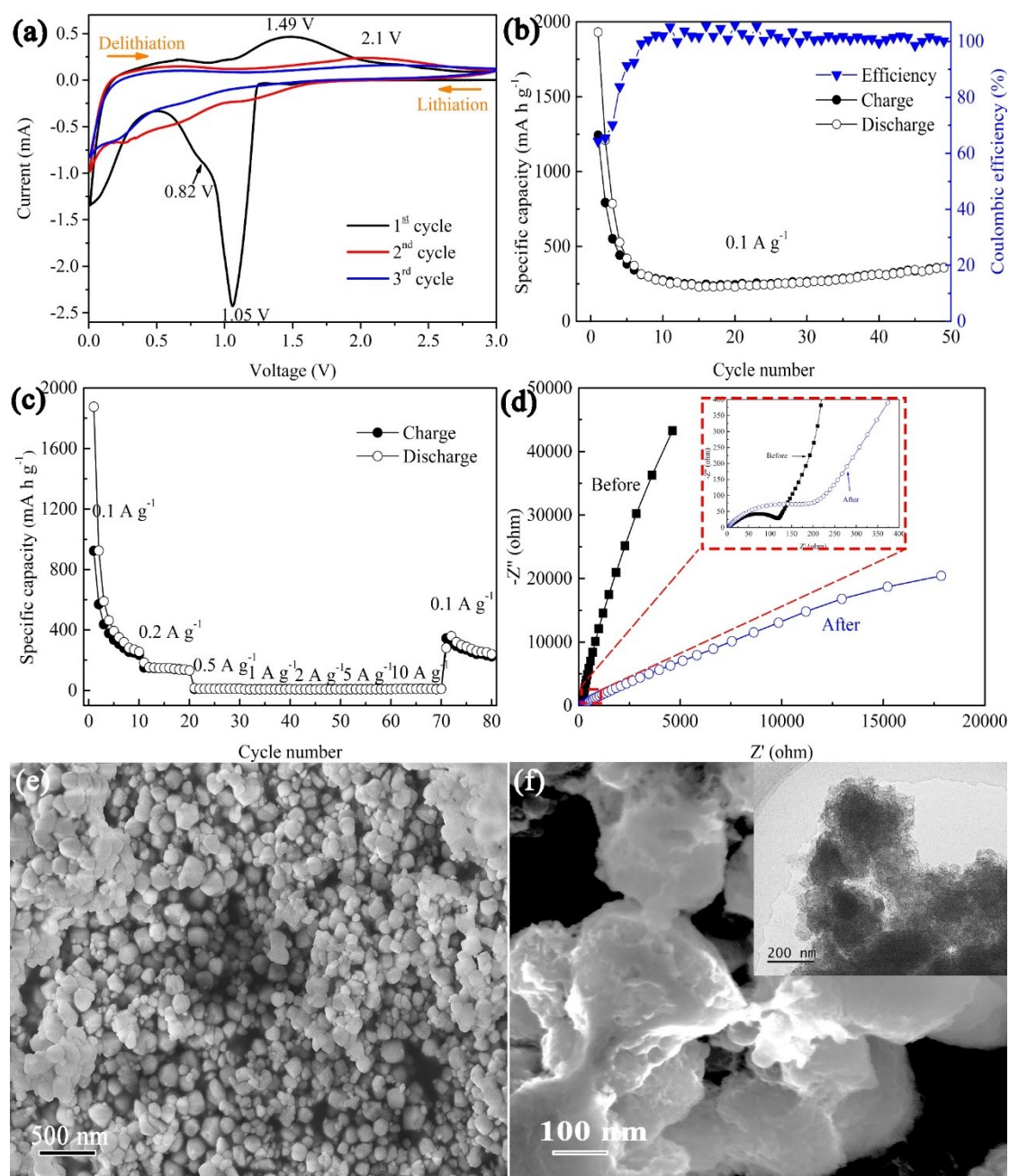


Fig. S3 Electrochemical performance of the $\text{Ni}(\text{HCO}_3)_2$. (a) Cyclic voltammograms recorded at a scan rate of 0.1 mV s^{-1} ; (b) cycling performance at a current density of 0.1 A g^{-1} ; (c) rate capability at various current densities (from 0.1 A g^{-1} to 10 A g^{-1}); (d) Nyquist curves of electrochemical impedance spectra before cycling, after 50th cycle at 0.1 A g^{-1} ; (e) SEM image of $\text{Ni}(\text{HCO}_3)_2$, and (f) SEM (the inset TEM) image of the $\text{Ni}(\text{HCO}_3)_2$ electrode cycled after 50th cycle at 0.1 A g^{-1}

The CV curves (Fig. S3a) show that, in the first cycle, $\text{Ni}(\text{HCO}_3)_2$ electrode develops a broad cathodic reduction peak centered at 1.05 V , which can be attributed to the reduction of Ni^{2+} to metallic Ni following equations 1. The subsequent cathodic reduction peak located at about 0.8 V

might be contributed to the transfer from LiHCO_3 to Li_xC_2 ($x=0, 1, 2$), which is probably catalyzed by in-situ generated Ni-nanocrystals, following Equations 2. The anodic peak at about 1.45 V is ascribed to the reversible transfer from Li_xC_2 ($x=0\sim 2$) to LiHCO_3 . However, in the first cycle, the anodic peak of Ni^{2+} is low (at about 2.1V). It is different from $\text{Ni}(\text{HCO}_3)_2/\text{rGO}$ electrode. After the first cycle, the $\text{Ni}(\text{HCO}_3)_2$ electrode only displays one cathodic peak and one anodic peak at about 0.5~1 V and 2.1 V, which are mainly ascribed to the oxidation-reduction of nickel. In the subsequent cycle, we cannot see the peak of HCO_3^- to Li_xC_2 ($x=0\sim 2$). It is indicated that the further reduction of LiHCO_3 into lower valence carbide materials (i.e., Li_xC_2 , $x = 0\sim 2$) can not be catalyzed by nickel nanocrystals due to the structural degradation caused by the large volume change or the self-aggregation of the Ni/NiO nanoparticles. At the same time, the poor electrochemical performances further indicates that the pure $\text{Ni}(\text{HCO}_3)_2$ do not effectively maintain the structure during charge and discharge process (Fig. S3b) and show the poor rate performance (Fig. S3c) owing to the low intrinsic electron and ion conductivities. The Nyquist plots (Fig. S3d) for the electrodes are similar, which show one semicircle at the high-middle frequency region, and an inclined line in low frequency region. The diameter of the semicircle is depending on the interface contact and charge transfer resistance.² Obviously, the charge transfer resistance and the diffusion impedance for the $\text{Ni}(\text{HCO}_3)_2$ electrode are much larger than those for the 3D $\text{Ni}(\text{HCO}_3)_2/\text{rGO}$ material. In the SEM image (Fig. S3e) of the control prepared $\text{Ni}(\text{HCO}_3)_2$ without GO at the same hydrothermal environment, it can be seen that the shape of $\text{Ni}(\text{HCO}_3)_2$ nanostructures in the $\text{Ni}(\text{HCO}_3)_2$ without GO is also cube-like. In the SEM and TEM (inset) images of the $\text{Ni}(\text{HCO}_3)_2$ electrode cycled after 50th cycle at 0.1 A g⁻¹ (Fig. S3f), it can be seen that the nanoparticles of pure $\text{Ni}(\text{HCO}_3)_2$ agglomeration and inefficient electrolyte-electrode

contact.

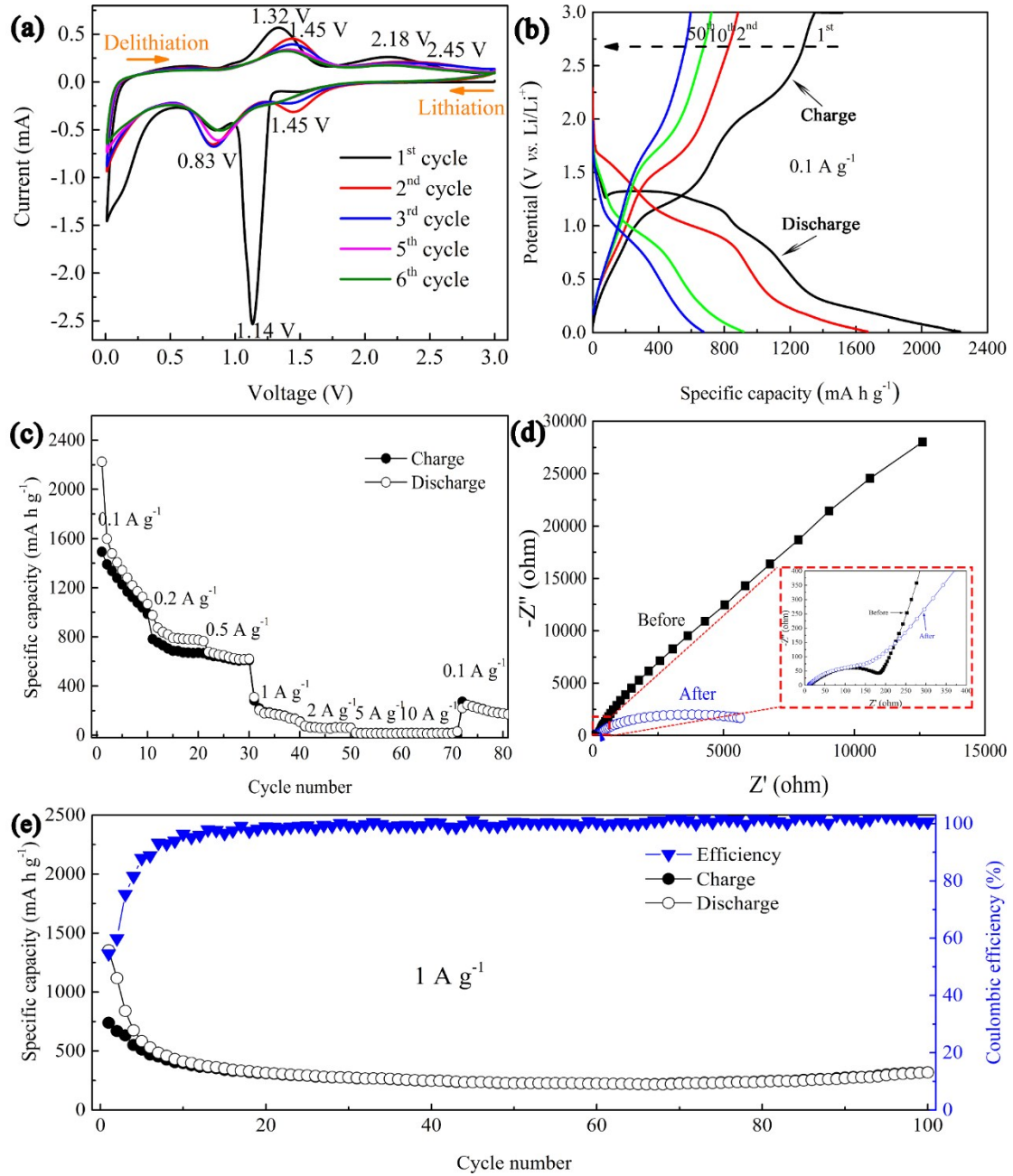


Fig. S4 Electrochemical performance of the mixed $\text{Ni}(\text{HCO}_3)_2@\text{rGO}$. (a) Cyclic voltammograms recorded at a scan rate of 0.1 mV s^{-1} ; (b) galvanostatic discharge/charge profiles of the 1st, 2nd, 10th, and 50th cycle at a current density of 0.1 A g^{-1} ; (c) rate capability at various current densities (from 0.1 A g^{-1} to 10 A g^{-1}); (d) Nyquist curves of electrochemical impedance spectra before cycling, after 50th cycle at a current density of 0.1 A g^{-1} ; (e) cycling performance at a current density of 1 A g^{-1} .

The sample fabricated by mechanically mixing rGO and $\text{Ni}(\text{HCO}_3)_2$ (denoted as $\text{Ni}(\text{HCO}_3)_2@\text{rGO}$) according to the same ratio as anodes were tested and compared with that of the 3D layered $\text{Ni}(\text{HCO}_3)_2/\text{rGO}$. To better investigate the reaction kinetics improved by the special 3D structure

of Ni(HCO₃)₂/rGO composite electrode, the cyclic voltammetry (CV) and charge-discharge profiles of Ni(HCO₃)₂@rGO are evaluated at a scan rate of 0.1 mV s⁻¹ and 0.1 A g⁻¹ in the voltage window of 0.01-3.0 V, respectively. As shown in Fig. S4a, in the first cathodic scan, a broad peak around 1.14 V can be clearly observed, which should be related to the reduction of Ni(HCO₃)₂ to Ni and the formation of activated LiHCO₃ (Eq. (1)), as well as the formation of solid electrolyte interface (SEI) layer. The subsequent cathodic reduction peak located at about 0.8 V might be contributed to the transfer from LiHCO₃ to Li_xC₂ (x=0, 1, 2). The sharp peak located at 0.01 V indicates the insertion of lithium into graphene. The oxidation peaks centered at 0.6 V, 1.32 V and 2.18 V in the corresponding anodic scan are due to the extraction of lithium from graphene, Li_xC₂ to LiHCO₃, and the oxidation of Ni to NiO, respectively. In the subsequent cycles, the new cathodic peak of 1.45 V shifts to lower voltage 1.3V, the cathodic peak of 0.83 V shifts to higher voltage 0.86 V, and the cathodic peak of 1.14 V disappears, while the anodic peaks of 1.32 V and 2.18 V shift to 1.45 V and 2.45 V, respectively. The CV curves can not overlap to each other, indicating that the bad cycle stability. The galvanostatic charge-discharge (GCD) curves (Fig.S4b) of the Ni(HCO₃)₂@rGO show high specific capacities of 2250 and 1510 mA h g⁻¹ in the first discharge and charge process, respectively, with a 67.1% coulombic efficiency. In the first discharge profile, a long potential plateau appears about 1.25 V, two weak potential plateau around 0.9 V and 0.05 V, which can be ascribed to reduction of Ni(HCO₃)₂ to Ni, LiHCO₃ to Li_xC₂, and the insertion of lithium into graphene, respectively. In the first charge profile, the potential plateau located at 1.3 V and 2.1 V corresponds to Li_xC₂ to LiHCO₃, and the oxidation of Ni to NiO, respectively. In the subsequent cycles, the discharge and charge profiles still cannot overlap, which is consistent with the CV results. Comparing the rate (Fig.S4c), EIS (Fig. S4d) and

cycle (Fig. S4e) performances of $\text{Ni}(\text{HCO}_3)_2@\text{rGO}$, the electrochemical performances of the 3D layered $\text{Ni}(\text{HCO}_3)_2/\text{rGO}$ are obviously infinitely superior to the mixed sample of $\text{Ni}(\text{HCO}_3)_2@\text{rGO}$.

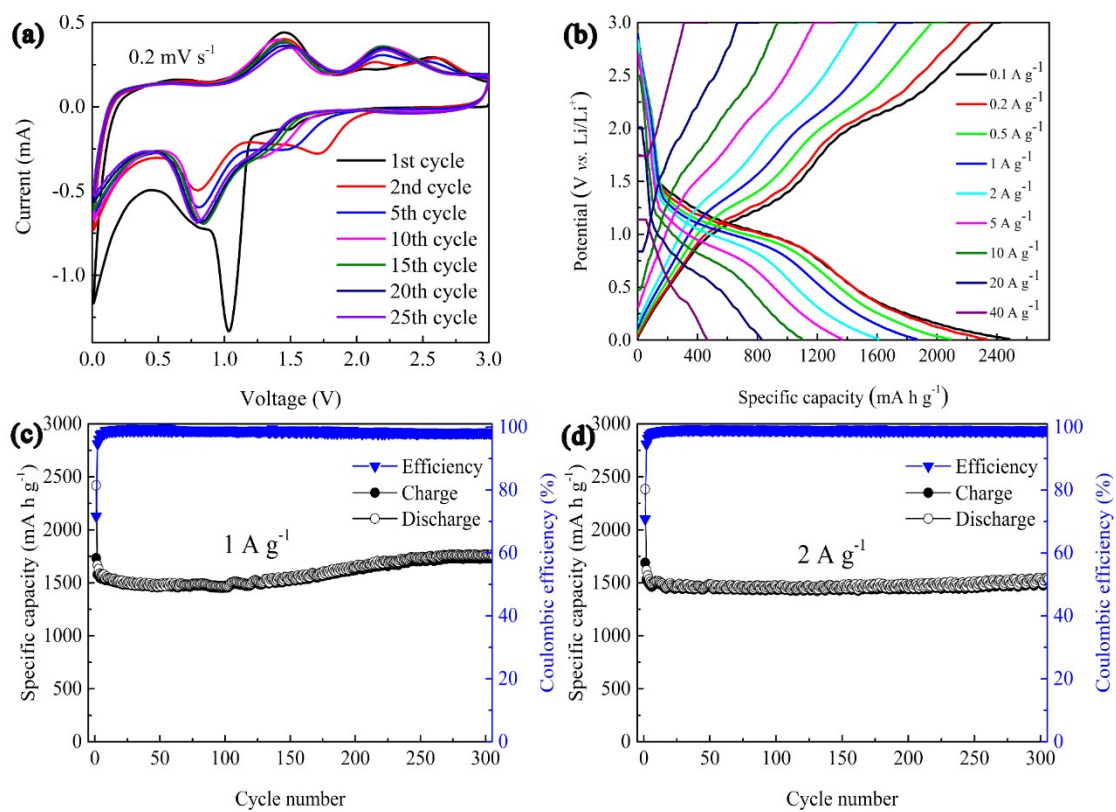


Fig. S5 (a) Cyclic voltammograms recorded at a scan rate of 0.2 mV s^{-1} (0.01 V-3 V), (b) voltage-capacity curves at different rates (increased from 0.1 A g^{-1} to 40 A g^{-1}); (c, d) cycling performances of the $\text{Ni}(\text{HCO}_3)_2/\text{rGO}$ electrodes at a current density of 1 and 2 A g^{-1} , respectively.

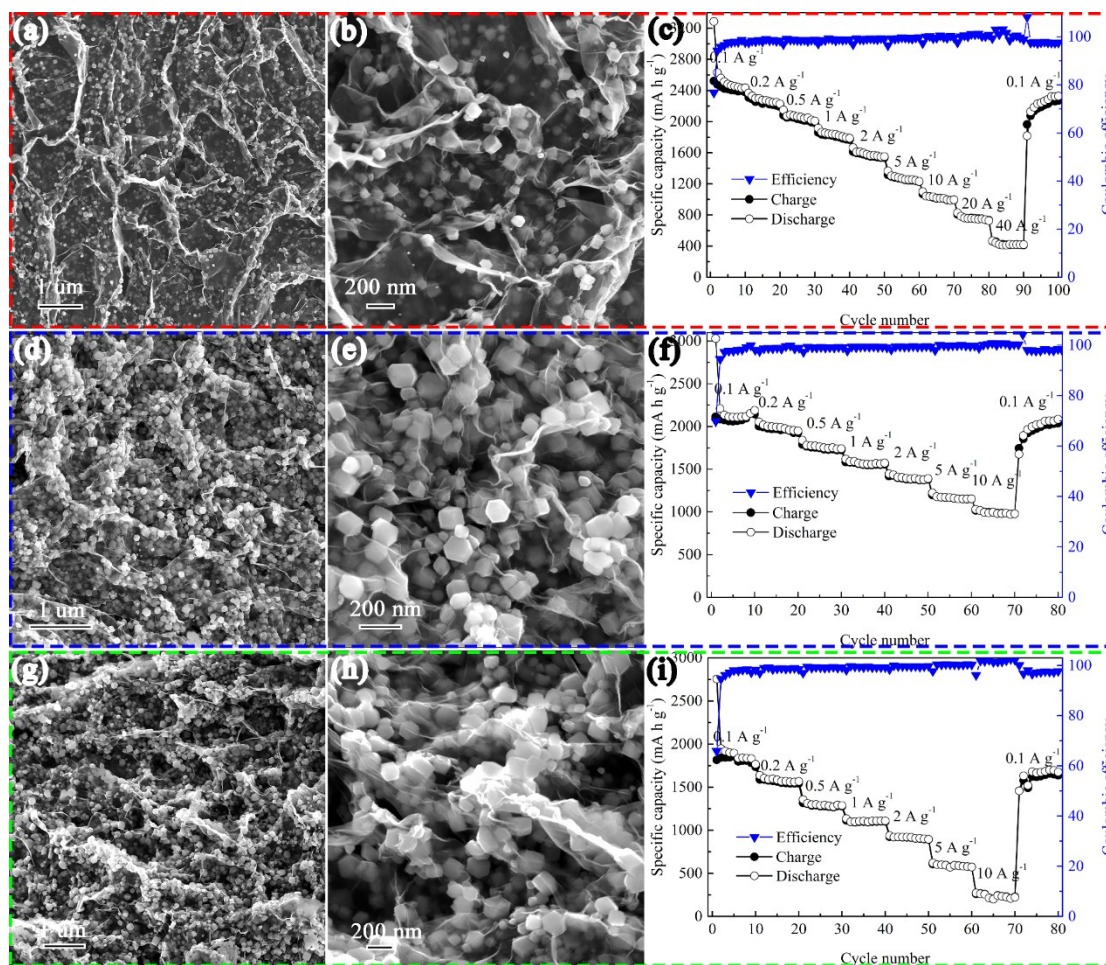


Fig. S6 SEM images and rate performances of the $\text{Ni}(\text{HCO}_3)_2/\text{rGO}$ at different nickel concentrations (GO, 1.5 mg mL^{-1}). (a-c) 0.02M , (d-f) 0.04M , and (g-i) 0.06M .

Since the GO films have confinement and hard template efficiency, the particle size of $\text{Ni}(\text{HCO}_3)_2$ nanocube is partly depend on the relative concentration of Ni^{2+} . As we all known that the size of the nanoparticle has an important influence on its electrochemical performance. We prepared the $\text{Ni}(\text{HCO}_3)_2/\text{rGO}$ composites using different concentrations of nickel source at the same concentration of GO (1.5 mg mL^{-1}). As the Fig. S6 shown, with increase of the nickel concentration, the sizes of the $\text{Ni}(\text{HCO}_3)_2$ nanocubes (Fig. S6a, b) seem to become little bigger on rGO films (Fig. S6d, e and Fig. S6g, h). And the $\text{Ni}(\text{HCO}_3)_2$ nanocubes can not be efficiently wrapped by the rGO films in relative higher concentrations of nickel ion. The experimental results in the different concentrations of nickel ion tell us that the 0.02M sample (Fig. S6a, b) displays the best rate property (Fig. S6c), when it is compared with the samples of 0.04M (Fig. S6f) and

0.06M (Fig. S6i).

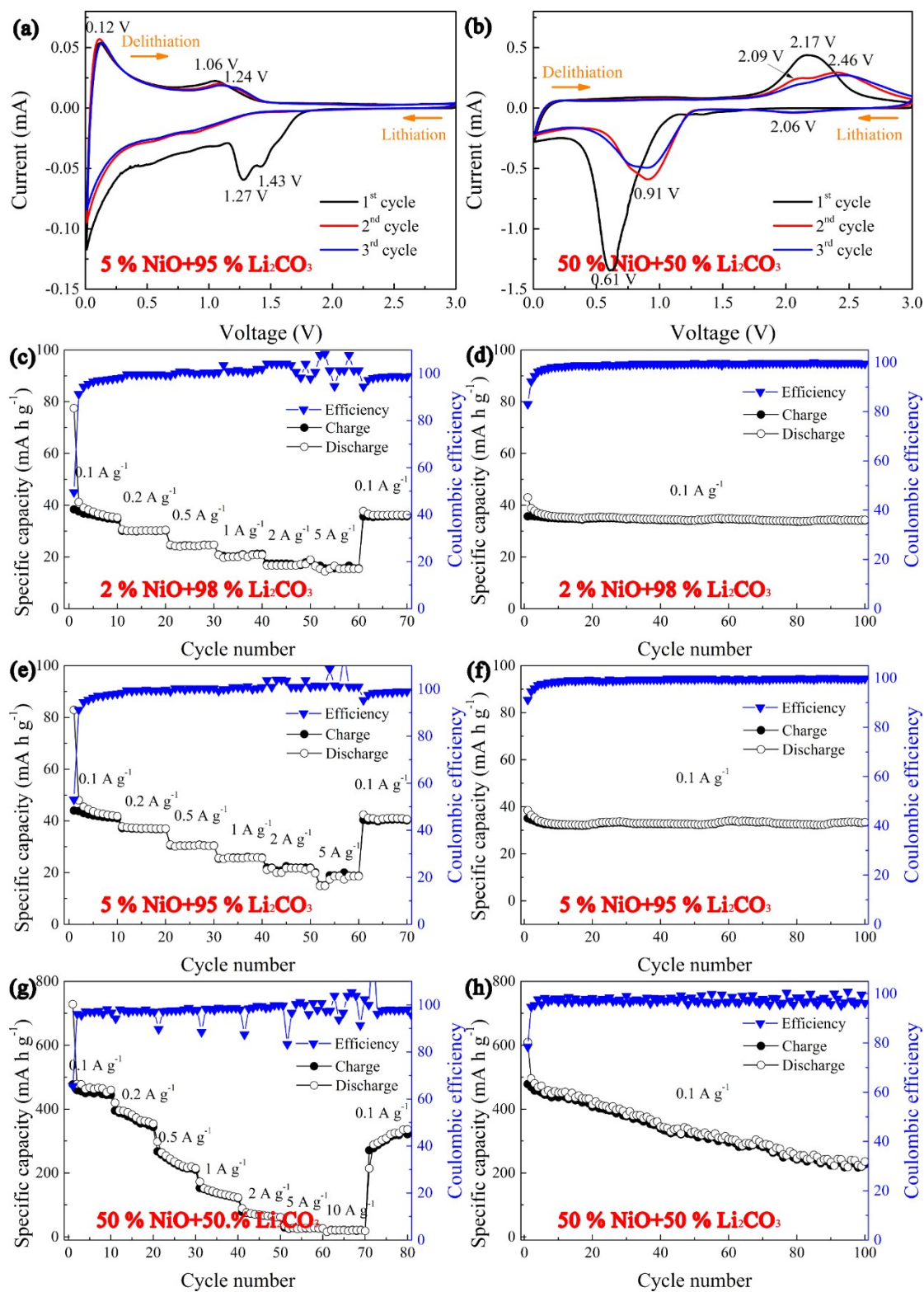


Fig. S7 Electrochemical performance of the mixtures of nano-nickel oxide and lithium carbonate at different proportions. (a, b) Cyclic voltammograms recorded at a scan rate of 0.1 mV s^{-1} ; (c, e, and g) rate capability and (d, f, and h) cycling performance for the mixtures at various proportions.

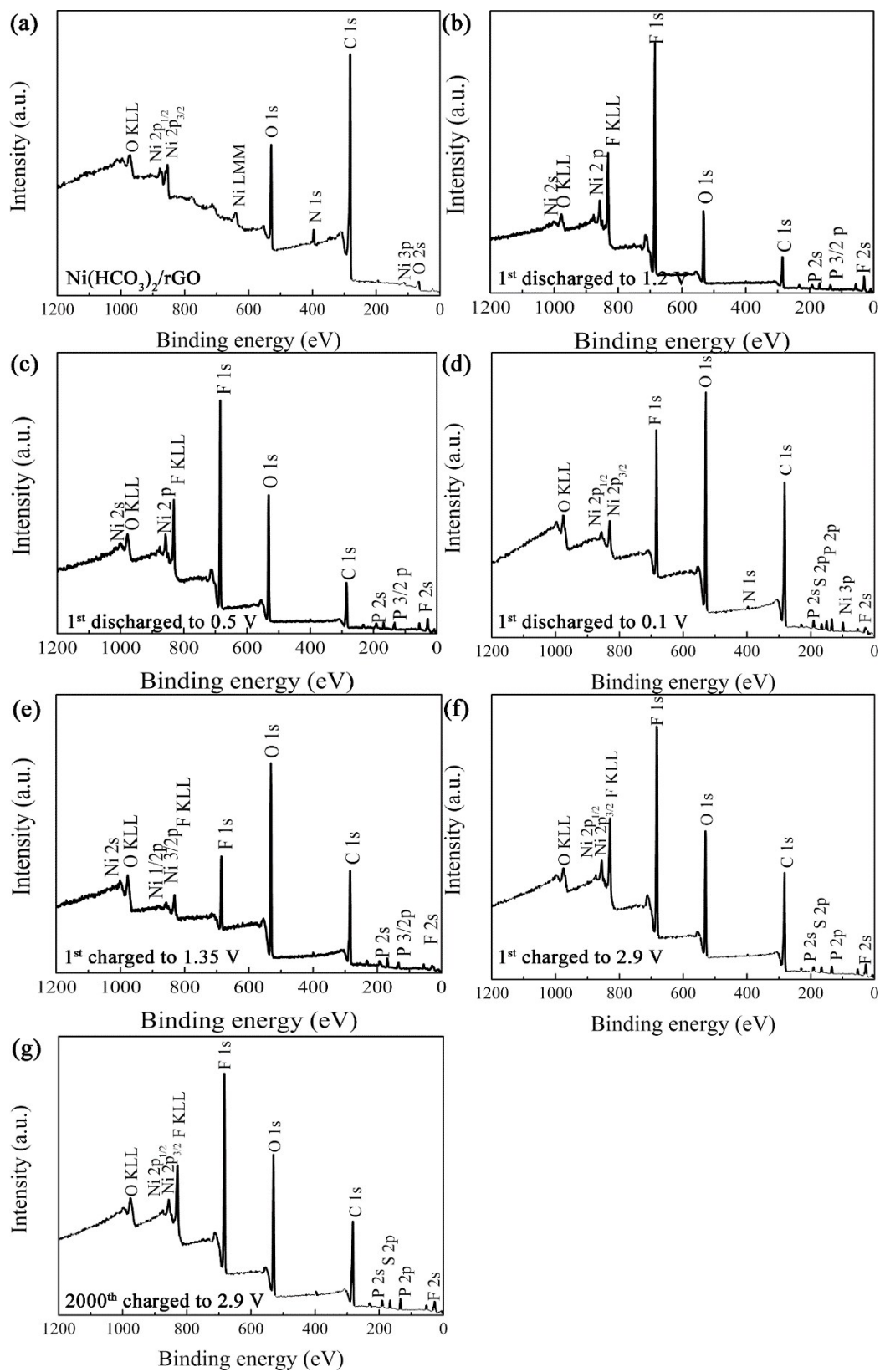


Fig. S8 Ex-situ XPS survey spectra of (a) Ni(HCO₃)₂/rGO, (b-d) different state electrodes of Ni(HCO₃)₂/rGO.

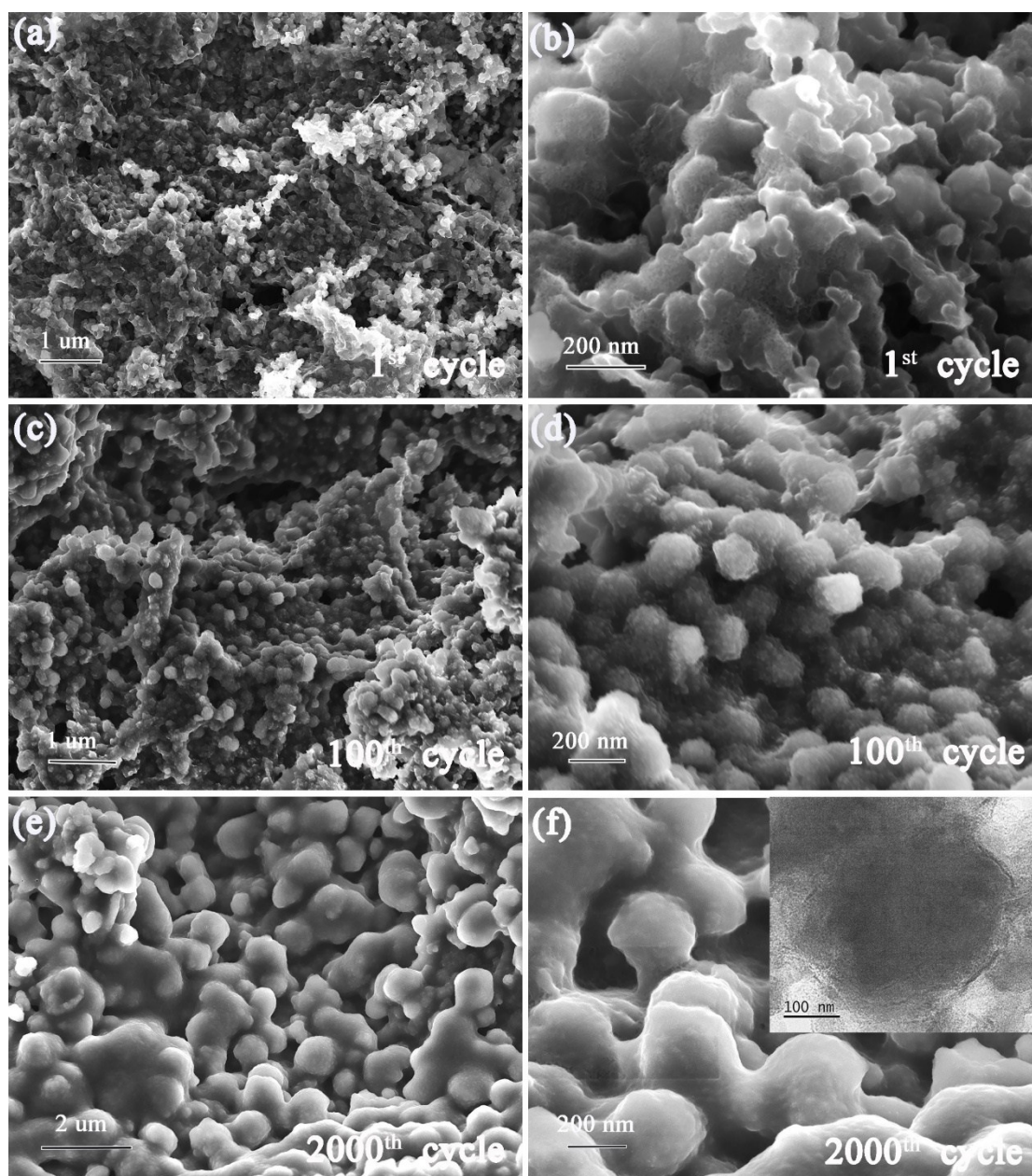


Fig. S9 (a-d) SEM images of Ni(HCO₃)₂/rGO electrodes cycled after different cycles at a current rate of 5 A g⁻¹, and (e, f) at a current rate of 10 A g⁻¹, the inset in f is TEM image.

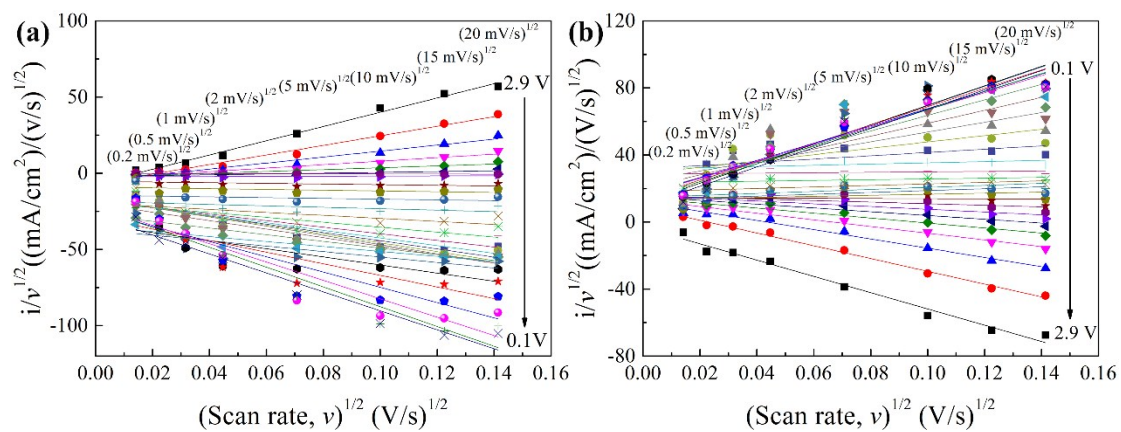


Fig. S10 Charts of the correlation between the $v^{1/2}$ and $i/v^{1/2}$. Use of equation $i(V)/v^{1/2} = k_1v^{1/2}+k_2$ to analyze the (a) cathodic and (b) anodic voltammetric sweep data for the $\text{Ni}(\text{HCO}_3)_2/\text{rGO}$ electrode: The voltage windows were chose from 2.9 V to 0.1 V (voltage interval is 0.1 volts) and the sweep rates were varied from 0.2 to 20 mV s^{-1} .

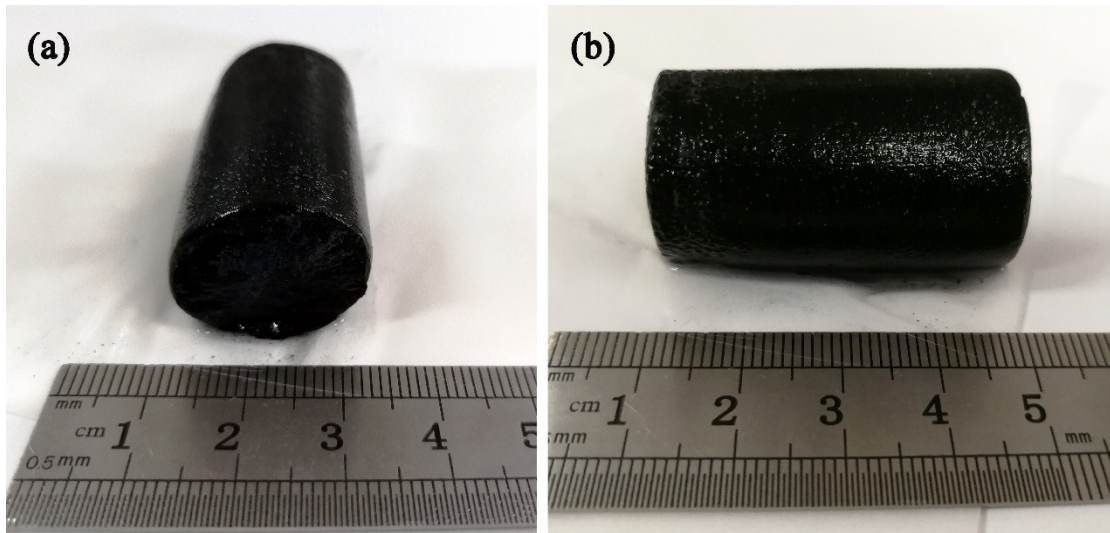


Fig. S11 The black cylindrical hydrogel pictures of the $\text{Ni}(\text{HCO}_3)_2/\text{rGO}$.

Table S1 The fitted parameters of the Ni(HCO₃)₂/rGO electrodes from the equivalent electrical circuit.

Element (Unit)	before cycling		After 80 cycles		After 2000 cycles	
	Value	Error (%)	Value	Error (%)	Value	Error (%)
Re (Ω)	2.401	8.7609	3.643	2.2901	7.144	1.8933
CPE-T(F)	8.75E-6	22.867	5.2875E-7	23.879	3.697E-6	20.495
CPE-P	0.825	6.065	1.054	2.0554	0.919	0.0475
R_{ct} (Ω)	31.54	23.295	5.775	3.7399	3.412	8.2072
Z_w (Ω)	112.8	5.4143	97.72	3.5399	57.3	2.899

Reference

1. Y. Dong, D. Li, C. Gao, Y. Liu and J. Zhang, *J. Mater. Chem. A*, 2017, **5**, 8087-8094.
2. H. Liu, Z. Hu, Y. Su, H. Ruan, R. Hu and L. Zhang, *Applied Surface Science*, 2017, **392**, 777-784.